Letter

Transition from a Biomimetic Molecular Switch to a Rotary Molecular Motor

Marco Paolino,* Tommaso Giovannini, Madushanka Manathunga, Loredana Latterini, Giulia Zampini, Robin Pierron, Jérémie Léonard, Stefania Fusi, Gianluca Giorgi, Germano Giuliani, Andrea Cappelli, Chiara Cappelli, and Massimo Olivucci*

Cite This: https://doi.org/10.1021/acs.jpclett.1c00526

Read Online

ACCESS | Metrics & More | Article Recommendations | SI Supporting Information

ABSTRACT: The experimental investigation of the unidirectional motion characterizing the photoisomerization of single-molecule rotary motors requires accessible lab prototypes featuring an electronic circular dichroism (ECD) signal that is sensitive to the geometrical and electronic changes occurring during an ultrafast reactive process. Here we report a combined experimental/computational study of a candidate obtained via the asymmetrization of a light-driven biomimetic molecular switch. We show that the achieved motor has an ECD band that is remarkably sensitive to the isomerization motion, and it is therefore suitable for time-resolved ECD studies. However, we also find that, unexpectedly, the synthesized motor isomerizes on a time scale longer than the subpicosecond time measured for the achiral parent, a result that points to alternative candidates conserving a high reaction speed.
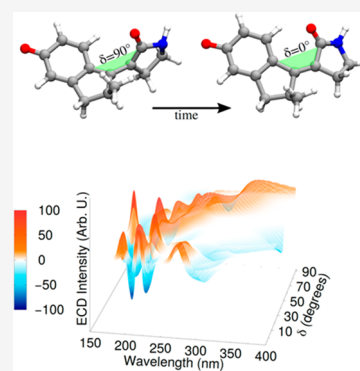
Natural molecular motors are nanometer macromolecular assemblies that are capable of converting chemical energy into mechanical motion.[1−3] These biological "devices" inspired the design and synthesis of subnanometer molecular motors that are expected to play a pivotal role in the development of artificial nanodevices[4−8] by converting chemical or light energy into directional motion of specific molecular or supramolecular parts.[9,10] In the work presented here, we focus on single-molecule rotary motors fueled by light-driven isomerizations of an asymmetric (i.e., chiral) olefin framework.[11] More specifically, these systems are capable of achieving the full rotation of a moiety called the "rotor" with respect to a fixed "stator" via consecutive Z-to-E and E-to-Z unidirectional (i.e., either clockwise or counterclockwise) photoisomerizations of a specific C=C bond separated by conformational helix-inversion steps.[6]

In the past, researchers have sought ways to design fast rotary motors and to measure the rotational direction and speed of the rotor.[12−15] Fast rotors are needed because, while a slow motor has the advantage of allowing a study of the rotation via stationary spectroscopies, only a high rotational speed is suitable for applications requiring synchronous rotations at the population level.[16−20] To achieve this, thermally randomized motion must be avoided by designing motors with low or absent thermal helix-inversion barriers; however, subpicosecond C=C isomerizations are also sought, with the expectation that they may enable a level of control of the rotational directionality and photoisomerization quantum yield similar to what was observed in the prototypical example of visual pigments.[21] Due to the chirality of rotary motors, time-resolved electronic circular dichroism (ECD) measurements would, in principle, allow one to follow a subpicosecond directional C=C twist. Such measurements represent a timely target as, in recent years, ECD has been implemented in pump−probe experiments, allowing the tracking of the variations of ultraviolet−visible (UV−vis) circular dichroism signals on the subpicosecond time scale.[22−24] In addition, pump−probe vibrational circular dichroism (VCD) has been developed in the mid-infrared spectral range to monitor the structural changes on the picosecond time scale.[25,26]

Over the past 10 years, we have been involved in the design, synthesis, and characterization of light-driven molecular switches (LDMSs), i.e., achiral systems that do not rotate unidirectionally. More specifically, we have used a biomimetic strategy to prepare positively charged N-alkylated or N-protonated indanylidene-pyrroline Schiff bases (NAIPs and NHIPs, respectively)[27−33] that mimic the subpicosecond C=C isomerization of the retinal chromophore of visual pigments.[34−36] A recent development led to a chiral NAIP derivative bearing a stereogenic center on the indene stator
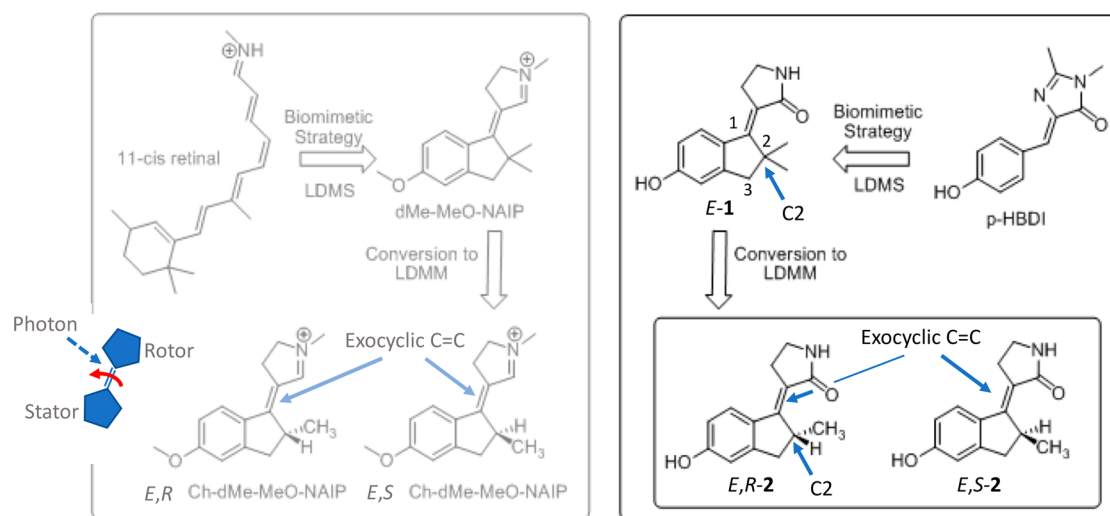
A

Figure 1. From LDMSs to chiral LDMMs. LDMMs miming the rhodopsin chromophore (left) and the GFP fluorophore (right), displayed as their *E* diastereoisomers. A schematic representation of a single-molecule rotary motor is shown on the left.

(Figure 1, left) and, thus, capable of biasing a cationic pyrroline rotor to rotate unidirectionally about the molecule's exocyclic C=C bonds.[37,38] Although the resulting Ch-dMe-MeO-NAIP system constitutes, in principle, a light-driven molecular motor (LDMM), it shows an overly weak ECD signal that is not suitable for experimental studies.[37]

With the hope of achieving the preparation of a subpicosecond rotating LDMM with a strong ECD signal, we present complementary experimental and computational studies of a chiral derivative of biomimetic light-driven LDMS **1** mimicking the *p*-hydroxybenzylidenedimethylimidazolone [*p*-HBDI (Figure 1, right)] fluorophore of the green fluorescent protein (GFP) and known to display a subpicosecond photoisomerization of both its *Z* and *E* diastereomers.[38] More specifically, we report on the design, synthesis, and characterization of LDMM **2** in racemic form, produced from **1** by inserting a stereogenic center into its stator to bias the rotation direction about the isomerizing C=C bond. By combining steady-state and transient UV−vis spectroscopies with computational studies carried out using two different levels of theory, we show that **2** represents a suitable lab model for future time-resolved ECD studies of the unidirectional rotary motion. The results are presented and discussed below where we sequentially deal with preparation, spectroscopic characterization, and computational studies of equilibrium and nonequilibrium structures. Whenever possible, the properties of **2** are compared with those reported for the homologue achiral compound **1**.[38]

Promotion to the first singlet excited state (S_1) of the anionic form of **1** triggers a charge translocation from the phenolic oxygen of the indene moiety (the stator) toward the pyrrolidone head (the rotor) unlocking the exocyclic C=C bond that isomerizes on the desired subpicosecond time scale.[38] Thus, to turn LDMS **1** into a LDMM, we decided to include a stereogenic center, expected to bias the rotation direction without changing the electronic structure of the molecule. As shown in Figure 1, this has been accomplished by "removing" one of the two C2 methyl substituents of **1**.

Compound **2** was synthesized starting from the available 5-methoxy-2-methyl-1-indanone using the strategy shown in Scheme 1. The racemic mixture of **4** was reacted with N-Boc-pyrrolidinone (**3**) to obtain the *E* and *Z* isomers of **6** (47%

Scheme 1[a]
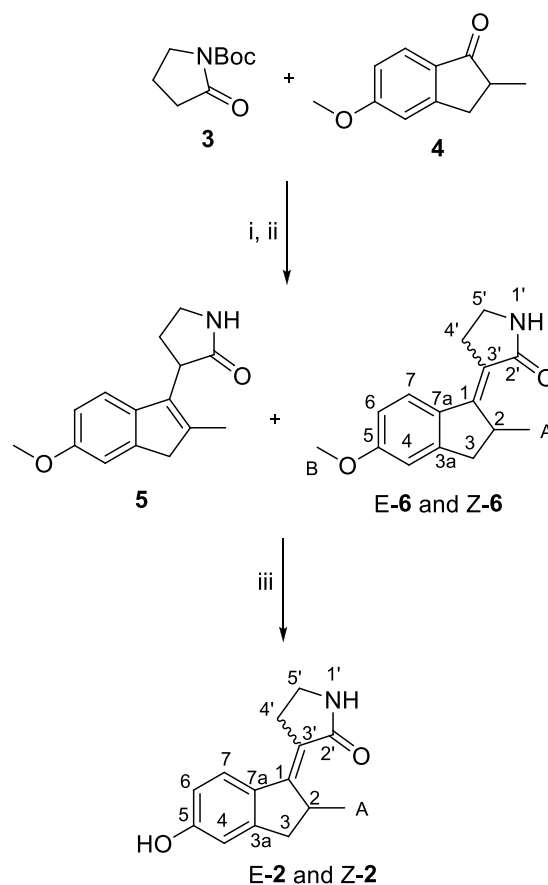
[a](i) N-Boc-pyrrolidinone, LiHDMS, BF$_3$(Et)$_2$O, THF; (ii) TFA, CH$_2$Cl$_2$; (iii) BBr$_3$, CH$_2$Cl$_2$.

yield, 8:2 *E*:*Z* ratio) by dehydration of the aldol condensation intermediate with TFA. The presence of only one methyl group in C2 (see Scheme 1 for the numbering) of the 5-methoxy-2-methyl-1-indanone led to the formation of undesired compound **5** (47% yield) due to the competition between the endo- and exocyclic dehydration of the

114 intermediate alcohol. However, the deprotection of the
115 methoxy group in both compounds **5** and **6** by reaction with
116 BBr$_3$ led to **2** as *E* and *Z* isomers both in a racemic mixture.
117 The structure of **2** has been characterized by homonuclear (^{1}H
118 and ^{13}C) and heteronuclear (^{1}H−^{1}H and ^{1}H−^{13}C) nuclear
119 magnetic resonance (NMR) analysis. In particular, NOE
120 experiments have been used to discriminate between the *E* and
121 *Z* configurations. In fact, contacts between H4′ and H7 were
122 observed in the dominant diastereoisomer and contacts
123 between H4′ and HA in the minor one, allowing the
124 assignment of the configurations to *E* and *Z*, respectively.
125 Moreover, the chemical structures of chiral intermediates **5**, *E*-
126 **6**, and *Z*-**6** in racemic form were confirmed by X-ray
127 crystallography (Figure SI-1) while **2** does not crystallize.
128   We now report on the stationary UV−vis, photochemical,
129 and ECD characterization and on the transient UV−vis
130 characterization of **2**, while the related computational studies
131 are presented below. An HPLC setup equipped with a
132 semipreparative column (Phenomenex Lux 5 μm Cellulose-1,
133 LC column, 250 mm × 4.6 mm) and applying *n*-hexane with
134 traces (3%) of isopropyl acid as the mobile phase was used to
135 separate the *E* and *Z* diastereomers of **2** in their neutral form.
136 The absorption spectra of the pure diastereomers were then
137 recorded in *n*-hexane (Figure 2). The *Z*-**2** band was found to
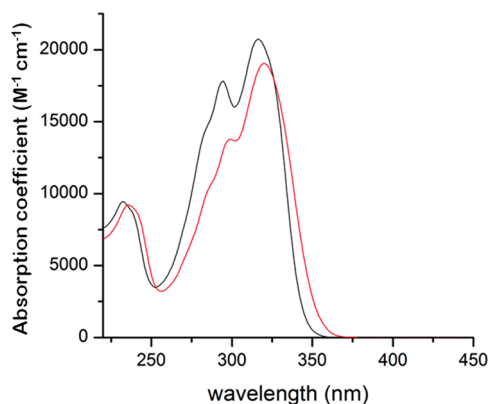138 be red-shifted with respect to the *E*-**2** band.

Figure 2. Quantitative absorption spectra of *E*-**2** (black) and *Z*-**2** (red) in *n*-hexane.

139   Similar to that of *E*-**1**,[38] the absorption spectrum of *E*-**2** was
140 recorded at pH values stabilizing the neutral and anionic forms
141 and in different solvents (Figure 3). The wavelengths of the
142 absorption maxima (λ_{max}) are listed in Table 1. In methanol
143 (Figure 3, red line), the neutral form of *E*-**2** shows two
144 dominant spectral components at 295 and 318 nm, and they
145 are therefore close to those reported for *E*-**1** [297 and 320 nm
146 (Figure 3, blue line)]. The two components do not display
147 significant solvatochromic effects (3−7 nm difference in λ_{max})
148 when hexane is replaced with methanol, dimethyl sulfoxide
149 (DMSO), acetonitrile, or water (see the Supporting
150 Information for the absorption spectra in acetonitrile and
151 water). In contrast, the spectrum of the corresponding anionic
152 form in methanol is characterized by a single band [λ_{max} = 347
153 nm (Figure 3, dashed red line)] significantly red-shifted with
154 respect to the neutral form in line with what reported for *E*-**1**
155 [λ_{max} = 351 nm (Figure 3, blue line)]. In contrast with its
156 neutral form, the anionic form of *E*-**2** shows a significant
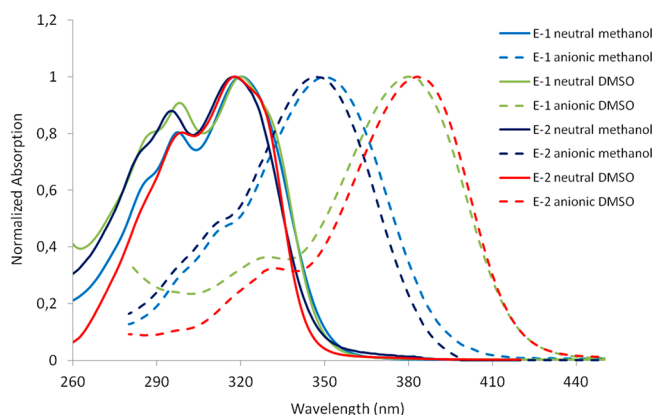157 solvatochromic effect when passing from methanol to DMSO

Figure 3. Normalized absorption spectra of the neutral (solid lines) and anionic (dashed lines) forms of *E*-**2** in methanol (red) and DMSO (orange) compared to the spectra of the neutral (solid blue line) and anionic (dashed blue line) forms of *E*-**1** in methanol.

Table 1. Absorption Maxima (λ_{max} values) of Neutral and Anionic *E*-2 in Different Solvents and PSS Composition of Neutral and Anionic 2 in Methanol at Different Irradiation Wavelengths[a]

solvent [dipole moment (D)]	absorption maxima in various solvents	
	E-**2** neutral λ_{max} (nm)	*E*-**2** anion[b] λ_{max} (nm)
hexane	293, 320	[c]
methanol (1.70)	295, 318 (297, 320)[d]	347 (351)[e]
water (1.85)	294, 317 (296, 319)[d]	345 (348)[e]
acetonitrile (3.92)	292, 312	362
DMSO (3.96)	299, 318 (298, 320)[d]	383 (381)[e]
Photostationary States in Methanol		
irradiation wavelength (nm)	*E*:*Z* composition (±0.1)	
Neutral Form		
290	1:0.89	
320	1:0.69	
360	1:0.30	
Anionic Form		
320	1:1.12	
350	1:0.92	
410	1:0.25	

[a]The λ_{max} values for *E*-**1** are also given. [b]Generated by addition of KOH to the neutral solutions. [c]Not soluble. [d]The value of compound *E*-**1** in neutral form in parentheses. [e]The value of compound *E*-**1** in anionic form generated by addition of an excess of KOH to the solution in parentheses.

158 [36 nm red-shift (Figure 3)] or acetonitrile [15 nm red-shift
159 (Figure SI-3)]. The different behavior of the anionic form may
160 be related to the higher flexibility of its π-electron density when
161 related to the marked difference in the dipole moment of the
162 two solvents (1.70 for methanol and 3.96 for DMSO).
163   The photostationary state (PSS) of **2** was investigated by
164 irradiation in a Pyrex NMR tube at room temperature in
165 methanol-*d*$_4$ using three irradiation wavelengths. The PSS *E*:*Z*
166 ratio was determined using ^{1}H NMR spectroscopy [area ratio
167 of the aromatic signals (Table 1 and Figure SI-4)]. No
168 significant change in ratio was observed after storing the
169 achieved PSS composition in the dark for a few days,
170 suggesting a high energy barrier for thermal C=C isomer-
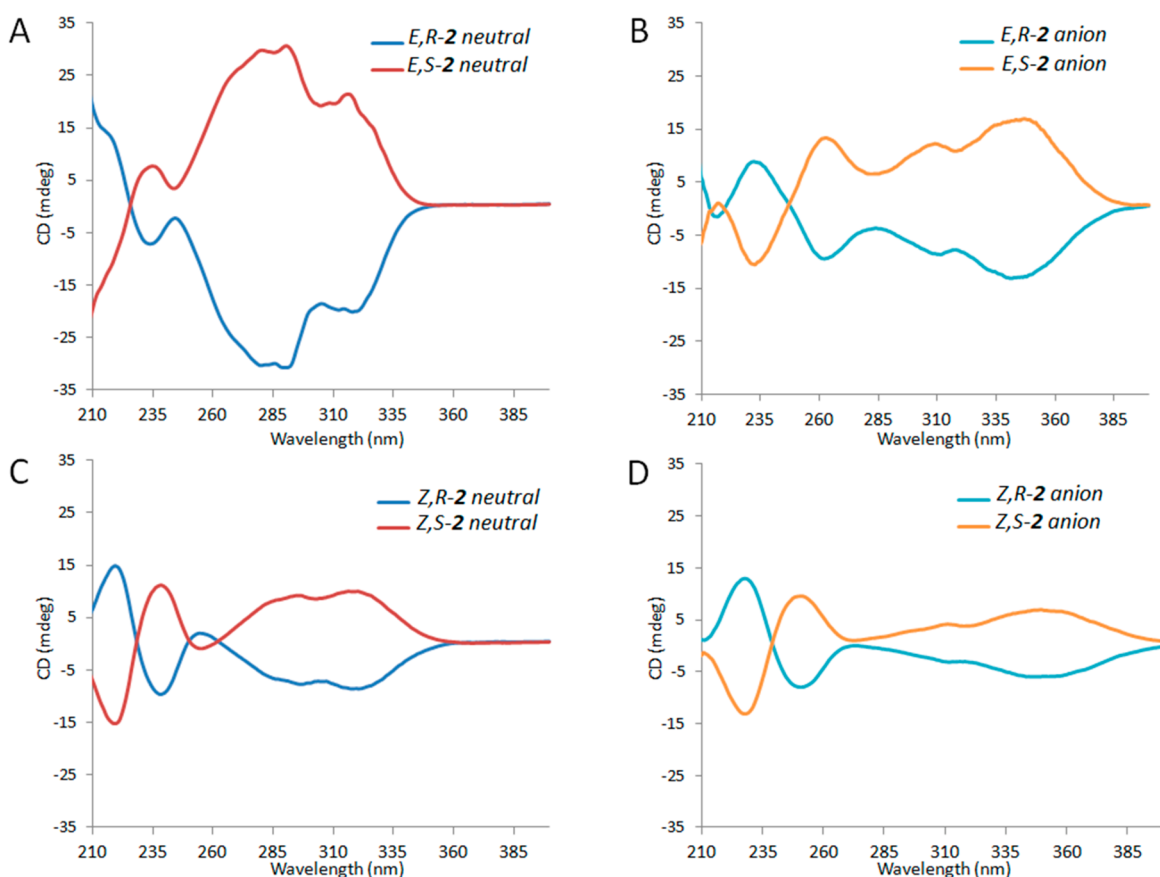171 ization at room temperature. Notice that an inversion of the

Figure 4. ECD spectra recorded in methanol of the two enantiomers of **2**. *E,R-***2** and *E,S-***2** in (A) neutral and (B) anionic form. *Z,R-***2** and *Z,R-***2** in (C) neutral and (D) anionic form.
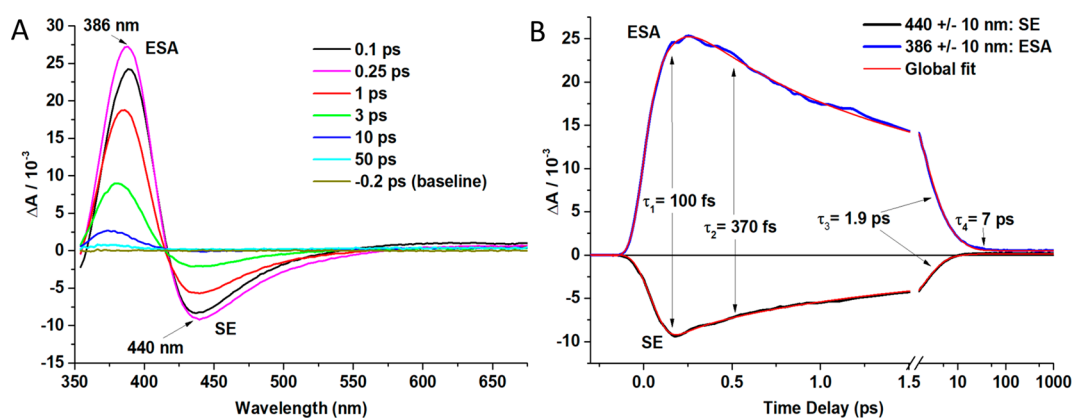

Figure 5. Transient absorption spectra. (A) Selected traces for the *E-***2** anion in methanol upon 350 nm excitation. (B) Transient absorption kinetic traces as a function of pump−probe time delay (in picosecond) observed at probing wavelengths of 386 nm. Both kinetic traces overlap with the result of the global, multiexponential fit (red lines). Four time constants ($\tau_1-\tau_4$) displayed on the graph are required for an accurate fit.

E:Z ratio could be achieved only when using the bluer 320 nm irradiation wavelength on the anionic form.

The absolute photoisomerization quantum yield of the neutral form of *E-***2** was determined to be 0.23 ± 0.01 in both methanol and *n*-hexane, as revealed by HPLC analysis and spectrophotometric measurements upon irradiation at 315 nm. Similarly, the medium-independent photoisomerization quantum yield value of 0.17 ± 0.01 was measured by spectrophotometric analysis upon irradiation at 350 nm for *E-***2** in the anionic form.

Using the HPLC setup described above, the *E,R-***2**, *E,S-***2** and *Z,R-***2** and *Z,S-***2** enantiomers were separated by employing a suitable chiral stationary phase. Thus, as reported in Figure 4, the ECD spectra of each enantiomer could be recorded for both the neutral and anionic forms obtained using KOH in a methanol solution (85 mM).

The spectra show distinctive features of the *E* or *Z* diastereoisomers that display, as expected, specular spectra for their enantiomers. The HPLC, ECD, and computational (see below for the *R* and *S* enantiomer assignment) analysis enables the assignment of the spectra of panels A and B of

D

Figure 4 to the E diastereoisomers, while the spectra of panels C and D of Figure 4 are assigned to the Z diastereoisomers. The fact that no racemization was observed upon deprotonation of the neutral forms enabled us to study also the anionic forms. The anion ECD spectra present broader and red-shifted bands. Furthermore, HPLC analysis shows that irradiation does not affect the enantiomeric purity.

For the photoisomerization dynamics of the anionic form, the investigation of the light-triggered dynamics of **2** was limited to the biomimetic anionic forms (i.e., this form mimics the GFP fluorophore). Accordingly, a methanol solution of a racemic mixture of the E-**2** anion (i.e., generated with an excess of KOH) was investigated via pump−probe, femtosecond transient absorption spectroscopy (TAS) with a resonant 350 nm pump pulse. A white-light femtosecond probe pulse was used to measure the time evolution of the absorption spectrum of the generated S_1 population with a time resolution of ∼60 fs and a spectral detection window from 350 to 600 nm (see experimental details and analysis procedures in ref 38). The resulting spectrum (see, e.g., the 0.25 ps spectrum in Figure 5A) displayed two bands. A positive band peaking around 386 nm was assigned to S_1 excited-state absorption (ESA, $S_1 \rightarrow S_n$ transition), and a negative band peaking at 440 nm was assigned to stimulated emission (SE, $S_1 \rightarrow S_0$ transition).

Inspection of the spectra reveals the following signatures. As compared to the 0.1 ps spectrum, in the 0.25 ps spectrum the ESA increases and slightly blue shifts while the SE slightly deepens in the range of 445−550 nm. This early S_1 relaxation is consistent with an overall SE red-shift attributed to vibrational and solvent relaxation. Then, in the 1 and 3 ps spectra, both SE and ESA decay significantly. At 10 ps, the SE band has completely vanished, and the positive band reaches a maximum at $\lambda \approx 375$ nm (i.e., at blue-shifted values with respect to the 386 nm maximum of the ESA at 0.25 ps). Because the SE has completely decayed, we assign the positive band to a photoproduct absorption (PA) corresponding to the vibrationally "hot" Z-**2** in the ground state (S_0). At 50 ps, the photoproduct has thermalized, and the residual signal corresponds to the difference absorption between E-**2** reactant and Z-**2** product spectra.

The quantitative analysis of the time evolution of these transient signatures was carried out by global fitting of the entire data set and is illustrated in Figure 5B at two probing wavelengths. The fitting produced four time constants. The shortest time constant ($\tau_1 = 100$ fs) characterizes the early spectral relaxation attributed to the initial vibrational and/or solvent relaxations. Two intermediate time constants ($\tau_2 = 370$ fs, and $\tau_3 = 1.9$ ps) were needed to fit the SE and ESA decay and are attributed to S_1 population biexponential decay kinetics. A longer time constant ($\tau_4 = 7$ ps) was required to fit further spectral relaxation in the UV range after S_1 decay and is assigned to thermalization of the hot S_0 population.

The main result of our TAS study is that two intermediate time constants, τ_2 and τ_3, describe the S_1 to S_0 decay, with the longest of the two time constants dominating [70% of the total S_1 decay amplitude monitored at 386 nm (see Figure 5B)]. Hence, an average S_1 decay time of 1.4 ps can be inferred. This is 10-fold longer than the S_1 lifetime of the achiral anion E-**1**,[39] where the dominating (90%) component was observed to be 120 fs, while a minor (10%) second decay time was found in the range of 0.4−0.8 ps.

As anticipated above, one would expect that a rotor embedded in an asymmetric environment rotates faster possibly due to a large initial out-of-plane distortion leading to a double bond pretwisting in S_0 and, in turn, a decrease in the S_1 lifetime. Such a correlation between an S_0 C=C pretwist and a faster C=C photoisomerization has been discussed in NAIP systems.[35] The observed increase in the S_1 lifetime of E-**2** with respect to E-**1** is therefore counterintuitive and calls for a conformational analysis that was carried out at the computational level (see below). Here we observe that the comparison of the crystallographic structures of the asymmetric E-**6** intermediate in Figure SI-1 and its formally symmetric analogue E-**7** (previously reported in ref 39) suggests that E-**2** and E-**1** are conformationally different (notice that it has not been possible to obtain suitable crystals for E-**2** and E-**1**). In fact, the removal of the methyl group at C2 must result in an increased planarity due to a reduced steric hindrance at the indanylidene stator level. As shown in Figure 6, the structure of E-**7** shows that C2 is lying outside the plane

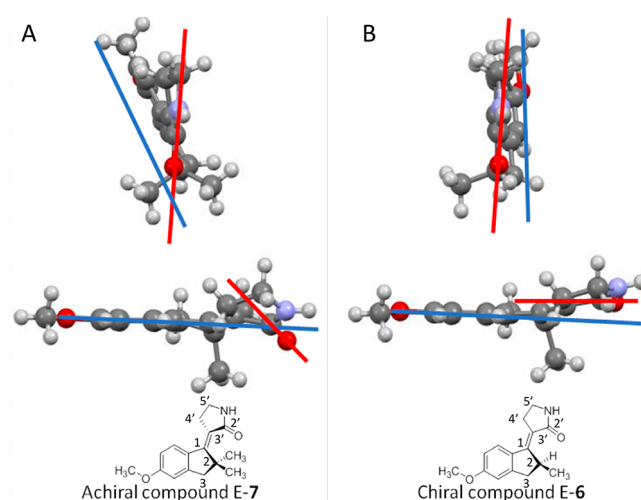**Figure 6.** Comparison of X-ray crystallographic structures of (A) achiral E-**7** and (B) chiral E-**6**.

of the aromatic ring of the indanylidene stator. Consequently, the pyrrolidinone rotor places its carbonyl oxygen in the middle of the two methyl groups at C2 of the stator (C1= C3'−C2'=O torsion angle of approximately −13°), forcing the rotor C4' out of the amide bond plane (C2'−N1−C5'− C4' torsion angle of approximately 6°). While a similar C2 placement is present in E-**6**, the reduced steric hindrance allows the carbonyl oxygen to interact with the hydrogen at C2 in a C=O−H−C contact (distance of 2.4 Å), also suggesting formation of an unconventional intramolecular hydrogen bond interaction (C1=C3'−C2'=O torsion angle of approximately −5.5°) that would further stabilize a planar framework. Notice that all atoms of the pyrrolidone moiety of E-**6** are located in approximately the same plane (C2'−N1−C5'−C4' torsion angle of −5.0°). Similarly, the pyrrolidinone head of E-**6** seems less strained than the pyrrolidinone head of E-**7**. Assuming that these conformational differences are maintained in E-**1** and E-**2**, the reduced helicity and, thus, C=C pretwist of E-**2** would be in line with a longer S_1 lifetime.

We then performed conformational analysis in solution and simulation of the stationary and transient ECD spectra. Following the TAS studies described above, we carried out two distinct computational investigations focusing, exclusively, on the anionic form of **2** and, for comparison, **1**. The S_0 room-

297 temperature conformational equilibrium (i.e., their Boltzmann
298 distribution) of E-**1** and E-**2** in methanol solution has been
299 simulated using a quantum-mechanics/molecular-mechanics
300 (QM/MM) model in which e the QM subsystem (the solute)
301 is treated using a multiconfigurational post-HF level of theory
302 (CASPT2//CASSCF/6-31G*) while the MM subsystem (the
303 solvent) is treated using the Amber force field.[40] Above, it has
304 been hypothesized that, counterintuitively, the stereogenic
305 center in E-**2** makes it more planar with respect to E-**1** due to a
306 reduced steric hindrance. To support this hypothesis, we have
307 employed our model to run classical molecular dynamics
308 (MD) at room temperature for both systems. The resulting
309 distributions, represented by a set of 400 uncorrelated
310 geometries and velocities (i.e., MD trajectory snapshots),
311 allow us to simulate the E-**1** and E-**2** absorption bands (see
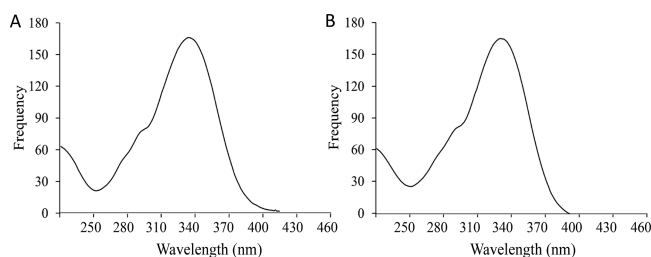312 Figure 7) by computing the corresponding 400 vertical

f7

Figure 7. Comparison between experimental (solid lines) and computed (histogram) absorption bands of the anionic forms of (A) achiral compound E-**1** and (B) chiral E-**2**.

313 excitation energy values. Therefore, we concluded that the
314 corresponding distribution of geometrical parameters as well as
315 their average values provides information about the solute
316 conformational structures.

317 In fact, encouraged by the fact that the computed λ_{max} values
318 (352 and 346 nm for E-**1** and E-**2**, respectively) are consistent
319 with the observed quantities of Table 1, we have estimated the
320 "planarity" of the E-**1** and E-**2** anions by looking at the values
321 of a set of dihedral angles (Figure 8). These include the C1=
322 C3′−C2′=O and C2′−N1−C5′−C4′ dihedral (see above)
323 and the C2′−C3′=C1−C2 dihedral describing the reactive
324 double-bond distortion from the point of view of the
325 pyrrolidinone rotor and of the C3a−C3−C2−C1, C2−C3−
326 C3a−C7a, and C3−C2−C1=C3′ dihedrals to evaluate the
327 stability of the stator. For E-**1**, the data show (Figure 8A,C) the
328 expected equilibrium between approximate mirror image
329 structures (i.e., the two enantiomeric conformations) display-
330 ing a helical framework in the stator and rotor portions.
331 However, for E,S-**2**, where the C2 stereogenic center is present,
332 only C2′−N1−C5′−C4′ dihedrals conserve a mirror image
333 aspect while C1=C3′−C2′=O and, most importantly, the
334 other dihedrals show that only one value of the dihedrals is
335 statistically dominant at equilibrium (Figure 8B−D). While
336 this points to the expected loss of one of the two equivalent
337 pseudomirror image conformers, we notice that (i) the
338 distribution becomes substantially broader and (ii) the chiral
339 E,S-**2** solute is substantially more planar than the achiral E-**1**
340 solute. This increased planarity confirms the hypothesis
341 proposed on the basis of the intermediate X-ray crystallo-
342 graphic structures seen above and points to a dominant E-**2**
343 planar conformation caused by the reduction in steric
344 hindrance.

345 An important comparison is that between the simulated
346 conformational equilibrium and the X-ray crystallographic
347 structures described above. For instance, it has been seen that
348 the experimental structures show C1=C3′−C2′=O dihedrals
349 of approximately −13° and −5.5° for the achiral and chiral
350 precursors, respectively. This result seems to be in line with the
351 data in the left graphs of panels A and B of Figure 8 that refer to
352 E-**1** and E-**2**, respectively. It is, in fact, evident that E-**1** displays
353 a broader angle distribution going from +15° to −15° while E-
354 **2** displays a narrower distribution centered around a −5°
355 angle. Consistently, the double bond torsion described by the
356 C2−C1=C3′−C2′ dihedral shows a broader and flat
357 approximately 9° to −9° distribution for E-**1** and a shaper
358 distribution for the chiral compound centered at 3° for E-**2**.

359 While we continue to focus on the anionic forms of E,S-**2**
360 and Z,S-**2** in methanol solutions, a different computational
361 model is employed to enable an ECD study. In fact, here we
362 employ a polarizable QM/MM approach, in which the QM
363 subsystem (the solute) is treated at the DFT level of theory
364 (CAM-B3LYP/6-311+G*) and the polarizable fluctuating
365 charge (FQ) force field is used for the MM subsystem (the
366 solvent).[41,42] As previously reported, such a QM/FQ model
367 can reliably simulate solvent effects on chiroptical proper-
368 ties.[43,44]

369 The QM/FQ ECD spectra were simulated to assign the
370 absolute configurations of the E-**2** and Z-**2** enantiomers based
371 on experimental spectra in panels B and D of Figure 4,
372 respectively. To do so, we extracted from the output of the MD
373 simulation discussed above for studying the room-temperature
374 equilibrium a set of 400 snapshots and computed the
375 corresponding ECD signal. The raw data arising from the
376 sampling are reported in the top graphs of panels A and B of
377 Figure 9. For both E-**2** and Z-**2**, the stick spectrum shows a
378 high variability in both excitation energy and sign of the
379 rotatory strength. Remarkably, it is found that similar
380 excitations can result in peak intensities of opposite sign that
381 can be attributed to the specific spatial arrangement of the
382 solvent around the solute and on the specific conformation of
383 the latter. The final QM/FQ spectrum is obtained by averaging
384 over the phase-space configurations, and it is reported in the
385 bottom graphs of panels A and B of Figure 9. The experimental
386 ECD spectra from panels B and D of Figure 4, now assigned to
387 the E,S-**2** and Z,S-**2** enantiomers of the anionic forms, are
388 reported in the same panels to facilitate comparison. Notice
389 that on this basis we also assign the absolute configuration of
390 the corresponding neutral forms.

391 The ECD spectrum of the E,S-**2** anion is characterized by a
392 (−,+,+,+) pattern resulting from a fine balance of sign
393 alternation (see the QM/FQ stick spectrum). The same
394 conclusions apply to the Z,S-**2** anion (see Figure 9B). For both
395 diasteroisomers, the QM/FQ model correctly predicts the
396 band broadening associated with each band, i.e., the
397 inhomogeneous band broadening arising from the sampling
398 of the phase space via MD. In both cases, the comparison
399 between experimental and QM/FQ spectra shows only small
400 discrepancies in peak relative intensities, which are probably
401 due to an incorrect description of high-energy excited states
402 provided by the selected DFT level. The agreement between
403 computed and experimental spectra is attributed to the correct
404 description of specific solute−solvent interactions, such as
405 hydrogen bonding (HB), and to correctly simulated conforma-
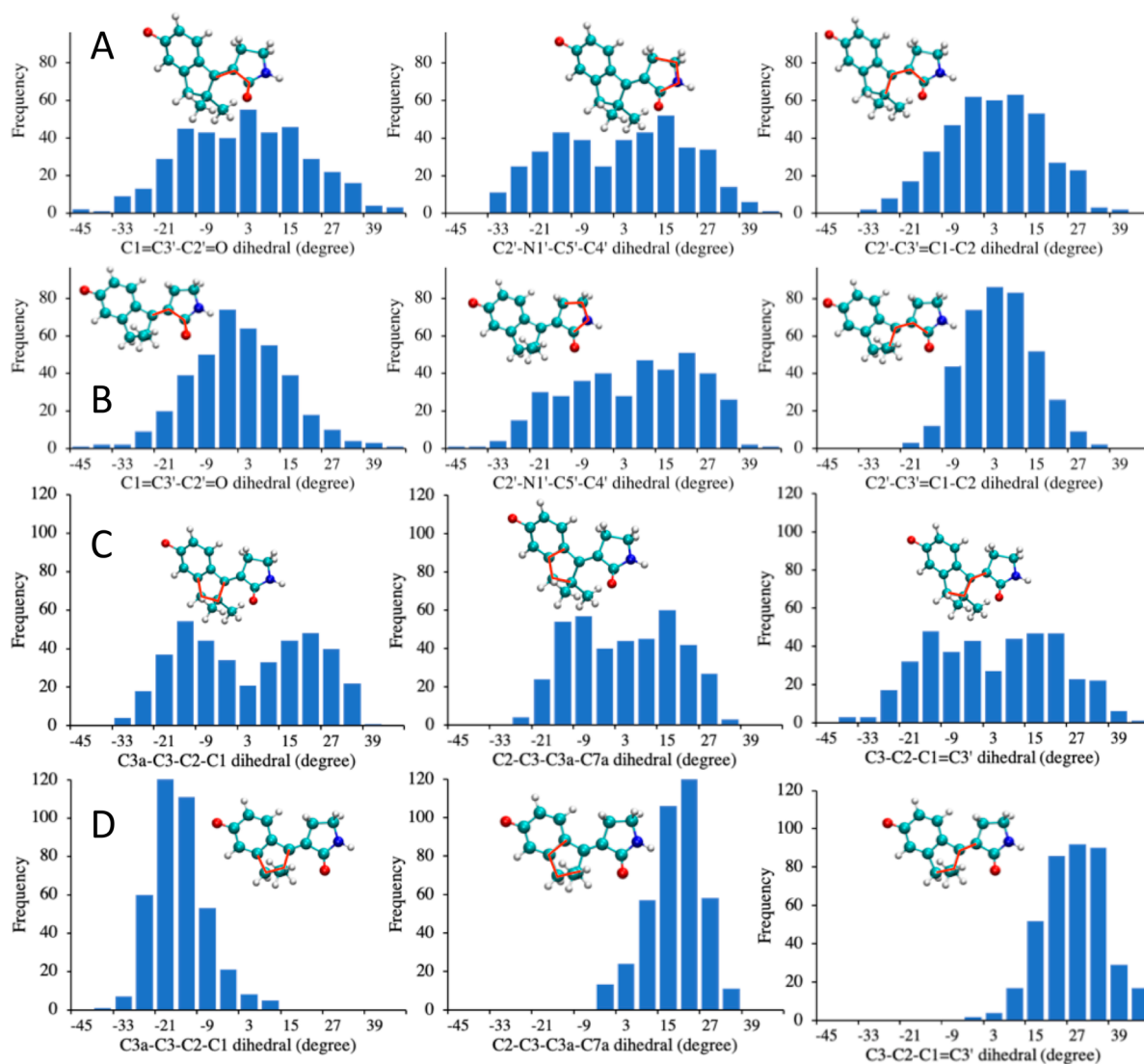406 tional freedom. In fact, as previously documented, these are

f8

f9

Figure 8. Comparison between the distribution of the dihedral angles describing rotor conformations for the anionic forms of (A) achiral *E*-**1** and (B) chiral *E,S*-**2** and of the dihedrals representing stator conformations of (C) achiral *E*-**1** and (D) chiral *E,S*-**2** in methanol solutions. In all cases, the dihedrals are indicated by a red segmented line on the corresponding molecular structure representation.
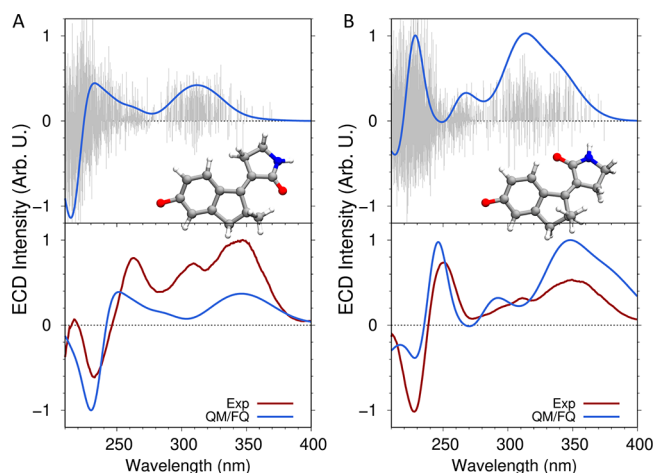

Figure 9. QM/FQ ECD spectra of anionic (A) *E,S*-**2** and (B) *Z,S*-**2** in methanol solutions. In both cases, raw data are shown as stick spectra (top panels). The convoluted QM/FQ spectra and their comparison with the measured spectrum are given in the bottom panels.

appropriately modeled by coupling the polarizable QM/FQ approach with MD runs.[45,46]

To assess the suitability of *E,S*-**2** as a lab model for future time-resolved ECD studies, we investigated the progression of the ECD spectra along the S_0 relaxation path populated immediately after S_1 decay at a S_1/S_0 conical intersection (CoIn) and leading to the *Z,S*-**2** product. For this reason, a CoIn has been first optimized at the QM/MM level starting from the already obtained *E,S*-**2** model. At such a CoIn, the reactive C=C bond is approximately 90° twisted [i.e., it is located halfway along the isomerization coordinate (see Figure 10A and Figure SI-4B)]. Accordingly, the QM/MM model defined above was used (i) to locate and optimize the CoIn and (ii) to propagate a QM/MM classical trajectory starting from the CoIn structure with zero initial velocities. To account for the extremely fast S_0 relaxation, the solvent has been kept frozen at the CoIn geometry during the downhill propagation.

ECD spectra in methanol were calculated along a collection of trajectory structures describing the S_0 relaxation toward the *Z,S*-**2** photoproduct. To do so, a QM/FQ model (see above) with the electronic degrees of freedom of the solvent (the FQ
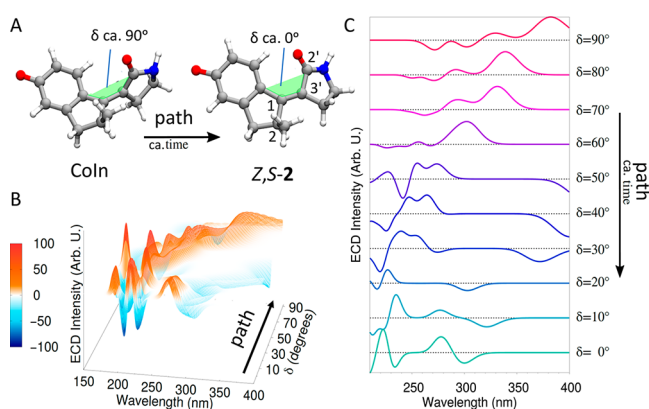
G

Figure 10. Evolution of computed QM/FQ ECD spectra along the S_0 relaxation path populated during *E,S*-**2** photoisomerization. (A) Schematic representation of the S_0 relaxation process in terms of the initial and final dihedral angle δ. (B) Computed QM/FQ ECD spectrum along the relaxation path. (C) Computed QM/FQ ECD spectra during the same process for selected values of δ.

charges) adjusted to the transition density was constructed for each path point. Thus, the ECD spectra are computed in a sort of non-equilibrium regime, with the solvent positions frozen, whereas the solute electronic degrees of freedom are left free to readjust. Such an assumption is justified by considering the time scales associated with the different reorganization processes.[47] The resulting ECD spectral evolution is reported in Figure 10B in terms of a two-dimensional plot as a function of the C2′−C3′═C1−C2 dihedral angle [δ (Figure 10A)]. QM/FQ-simulated ECD spectra for 10 selected dihedral angles are reported in Figure 10C. The results show that the spectrum undergoes dramatic changes during the photo-isomerization and indicate that such changes should be detectable via time-resolved ECD measurements. In other words, we conclude that transient ECD spectroscopy with sufficient time resolution is likely to be able to provide information about the photoisomerization of the prepared LDMM, possibly resolving the unidirectional rotation direction at the population level.

We have provided evidence that the asymmetrization of an anionic LDMS generates a prototype LDMM useful for transient ECD studies. In fact, a strong ECD band with a good signal-to-noise ratio demonstrates that **2** is a plausible model for ECD experiments. Furthermore, the successful comparison between simulated and observed stationary ECD spectra suggests that such experiments could be planned and integrated by QM/MM and QM/FC simulations. On the contrary, TSA studies have also shown that *E*-**2** features a substantial decrease in photoisomerization speed relative to that of its achiral LDMS analogue. Such a decrease (from 0.25 to 1.5 ps in terms of excited-state lifetime) is attributed to the planarization of the system framework following the removal of a methyl group in the region connecting the stator and rotor. This indicates that the replacement of one of the two methyl substituents of **1** with a larger (e.g., an ethyl or, better, isopropyl group), rather than smaller, group would lead to an ideal LDMM with a conserved or increased skeletal out-of-plane deformation (i.e., molecular helicity) and, therefore, isomerization speed.

■ ASSOCIATED CONTENT

ⓢ Supporting Information

The Supporting Information is available free of charge at https://pubs.acs.org/doi/10.1021/acs.jpclett.1c00526.

Synthesis, X-ray crystallography, photoisomerization quantum yields, ECD, simulation, generation of initial conditions, QM/fluctuating charge-QM/FQ, and additional references (PDF)

■ AUTHOR INFORMATION

Corresponding Authors

Marco Paolino − *Dipartimento di Biotecnologie, Chimica e Farmacia, Università di Siena, 53100 Siena, Italy;* ● orcid.org/0000-0003-1387-7875; Email: paomar@oneonline.it

Massimo Olivucci − *Dipartimento di Biotecnologie, Chimica e Farmacia, Università di Siena, 53100 Siena, Italy; Chemistry Department, Bowling Green State University, Bowling Green, Ohio 43403-0001, United States;* ● orcid.org/0000-0002-8247-209X; Email: molivuc@bgsu.edu

Authors

Tommaso Giovannini − *Scuola Normale Superiore, 56126 Pisa, Italy;* ● orcid.org/0000-0002-5637-2853

Madushanka Manathunga − *Chemistry Department, Bowling Green State University, Bowling Green, Ohio 43403-0001, United States;* ● orcid.org/0000-0002-3594-8112

Loredana Latterini − *Dipartimento di Chimica, Biologia e Biotecnologie, Università di Perugia, 06123 Perugia, Italy;* ● orcid.org/0000-0002-1021-9423

Giulia Zampini − *Dipartimento di Chimica, Biologia e Biotecnologie, Università di Perugia, 06123 Perugia, Italy;* ● orcid.org/0000-0002-2684-1604

Robin Pierron − *Université de Strasbourg, CNRS, Institut de Physique et Chimie des Matériaux de Strasbourg, UMR 7504, F-67000 Strasbourg, France*

Jérémie Léonard − *Université de Strasbourg, CNRS, Institut de Physique et Chimie des Matériaux de Strasbourg, UMR 7504, F-67000 Strasbourg, France*

Stefania Fusi − *Dipartimento di Biotecnologie, Chimica e Farmacia, Università di Siena, 53100 Siena, Italy*

Gianluca Giorgi − *Dipartimento di Biotecnologie, Chimica e Farmacia, Università di Siena, 53100 Siena, Italy;* ● orcid.org/0000-0002-8817-7745

Germano Giuliani − *Dipartimento di Biotecnologie, Chimica e Farmacia, Università di Siena, 53100 Siena, Italy*

Andrea Cappelli − *Dipartimento di Biotecnologie, Chimica e Farmacia, Università di Siena, 53100 Siena, Italy;* ● orcid.org/0000-0003-4140-3028

Chiara Cappelli − *Scuola Normale Superiore, 56126 Pisa, Italy;* ● orcid.org/0000-0002-4872-4505

Complete contact information is available at:
https://pubs.acs.org/10.1021/acs.jpclett.1c00526

Notes

The authors declare no competing financial interest.

H

■ REFERENCES

(1) Mallik, R.; Gross, S. P. Molecular Motors: Strategies to Get Along. *Curr. Biol.* **2004**, *14* (22), R971−R982.

(2) Schliwa, M.; Woehlke, G. Molecular Motors. *Nature* **2003**, *422* (6933), 759−765.

(3) Iino, R.; Kinbara, K.; Bryant, Z. Introduction: Molecular Motors. *Chem. Rev.* **2020**, *120* (1), 1−4.

(4) Chen, J.; Leung, F. K.-C.; Stuart, M. C. A.; Kajitani, T.; Fukushima, T.; van der Giessen, E.; Feringa, B. L. Artificial Muscle-like Function from Hierarchical Supramolecular Assembly of Photoresponsive Molecular Motors. *Nat. Chem.* **2018**, *10* (2), 132−138.

(5) Feringa, B. L. The Art of Building Small. *Chem. Int.* **2016**, *38* (5), 2−7.

(6) Roke, D.; Wezenberg, S. J.; Feringa, B. L. Molecular Rotary Motors: Unidirectional Motion around Double Bonds. *Proc. Natl. Acad. Sci. U. S. A.* **2018**, *115* (38), 9423−9431.

(7) Kassem, S.; van Leeuwen, T.; Lubbe, A. S.; Wilson, M. R.; Feringa, B. L.; Leigh, D. A. Artificial Molecular Motors. *Chem. Soc. Rev.* **2017**, *46* (9), 2592−2621.

(8) Zhang, Q.; Qu, D.-H.; Tian, H.; Feringa, B. L. Bottom-Up: Can Supramolecular Tools Deliver Responsiveness from Molecular Motors to Macroscopic Materials? *Matter* **2020**, *3* (2), 355−370.

(9) Le Poul, N.; Colasson, B. Electrochemically and Chemically Induced Redox Processes in Molecular Machines. *ChemElectroChem* **2015**, *2* (4), 475−496.

(10) Baroncini, M.; Silvi, S.; Credi, A. Photo- and Redox-Driven Artificial Molecular Motors. *Chem. Rev.* **2020**, *120* (1), 200−268.

(11) Koumura, N.; Geertsema, E. M.; van Gelder, M. B.; Meetsma, A.; Feringa, B. L. Second Generation Light-Driven Molecular Motors. Unidirectional Rotation Controlled by a Single Stereogenic Center with Near-Perfect Photoequilibria and Acceleration of the Speed of Rotation by Structural Modification. *J. Am. Chem. Soc.* **2002**, *124* (18), 5037−5051.

(12) Vicario, J.; Meetsma, A.; Feringa, B. L. Controlling the Speed of Rotation in Molecular Motors. Dramatic Acceleration of the Rotary Motion by Structural Modification. *Chem. Commun.* **2005**, No. 47, 5910−5912.

(13) Filatov, M.; Paolino, M.; Min, S. K.; Kim, K. S. Fulgides as Light-Driven Molecular Rotary Motors: Computational Design of a Prototype Compound. *J. Phys. Chem. Lett.* **2018**, *9* (17), 4995−5001.

(14) Filatov, M.; Paolino, M.; Min, S. K.; Choi, C. H. Design and Photoisomerization Dynamics of a New Family of Synthetic 2-Stroke Light Driven Molecular Rotary Motors. *Chem. Commun.* **2019**, *55* (36), 5247−5250.

(15) Roke, D.; Sen, M.; Danowski, W.; Wezenberg, S. J.; Feringa, B. L. Visible-Light-Driven Tunable Molecular Motors Based on Oxindole. *J. Am. Chem. Soc.* **2019**, *141* (18), 7622−7627.

(16) Feringa, B. L. The Art of Building Small: From Molecular Switches to Molecular Motors. *J. Org. Chem.* **2007**, *72* (18), 6635−6652.

(17) Chen, J.; Vachon, J.; Feringa, B. L. Design, Synthesis, and Isomerization Studies of Light-Driven Molecular Motors for Single Molecular Imaging. *J. Org. Chem.* **2018**, *83* (11), 6025−6034.

(18) Chen, J.; Chen, K.-Y.; Carroll, G. T.; Feringa, B. L. Facile Assembly of Light-Driven Molecular Motors onto a Solid Surface. *Chem. Commun.* **2014**, *50* (84), 12641−12644.

(19) van Leeuwen, T.; Lubbe, A. S.; Štacko, P.; Wezenberg, S. J.; Feringa, B. L. Dynamic Control of Function by Light-Driven Molecular Motors. *Nat. Rev. Chem.* **2017**, *1* (12), 96.

(20) Zhao, D.; van Leeuwen, T.; Cheng, J.; Feringa, B. L. Dynamic Control of Chirality and Self-Assembly of Double-Stranded Helicates with Light. *Nat. Chem.* **2017**, *9* (3), 250−256.

(21) Schoenlein, R. W.; Peteanu, L. A.; Mathies, R. A.; Shank, C. V. The first step in vision: femtosecond isomerization of rhodopsin. *Science* **1991**, *254*, 412−415.

(22) Meyer-Ilse, J.; Akimov, D.; Dietzek, B. Recent Advances in Ultrafast Time-Resolved Chirality Measurements: Perspective and Outlook. *Laser Photon. Rev.* **2013**, *7* (4), 495−505.

(23) Auvray, F.; Dennetiere, D.; Giuliani, A.; Jamme, F.; Wien, F.; Nay, B.; Zirah, S.; Polack, F.; Menneglier, C.; Lagarde, B.; et al. Time Resolved Transient Circular Dichroism Spectroscopy Using Synchrotron Natural Polarization. *Struct. Dyn.* **2019**, *6* (5), 054307.

(24) Steinbacher, A.; Hildenbrand, H.; Kramer, C.; Schäferling, M.; Giessen, H.; Brixner, T. Chirality-Sensitive Ultrafast Spectroscopy. In *International Conference on Ultrafast Phenomena*; Optical Society of America, 2016; p UM3A.1. DOI: 10.1364/UP.2016.UM3A.1

(25) Bonmarin, M.; Helbing, J. Picosecond Time-Resolved Vibrational Circular Dichroism Spectroscopy. In *Ultrafast Phenomena XVI*; Corkum, P., Silvestri, S., Nelson, K. A., Riedle, E., Schoenlein, R. W., Eds.; Springer: Berlin, 2009; pp 391−393.

(26) Bonmarin, M.; Helbing, J. A Picosecond Time-Resolved Vibrational Circular Dichroism Spectrometer. *Opt. Lett.* **2008**, *33* (18), 2086−2088.

(27) Zanirato, V.; Pollini, G. P.; De Risi, C.; Valente, F.; Melloni, A.; Fusi, S.; Barbetti, J.; Olivucci, M. Synthesis of Biomimetic Light-Driven Molecular Switches via a Cyclopropyl Ring-Opening/ Nitrilium Ion Ring-Closing Tandem Reaction. *Tetrahedron* **2007**, *63*, 4975−4982.

(28) Léonard, J.; Schapiro, I.; Briand, J.; Fusi, S.; Paccani, R. R.; Olivucci, M.; Haacke, S. Mechanistic Origin of the Vibrational Coherence Accompanying the Photoreaction of Biomimetic Molecular Switches. *Chem. - Eur. J.* **2012**, *18*, 15296−15304.

(29) Dunkelberger, A. D.; Kieda, R. D.; Shin, J. Y.; Rossi Paccani, R.; Fusi, S.; Olivucci, M.; Fleming Crim, F. Photoisomerization and Relaxation Dynamics of a Structurally Modified Biomimetic Photoswitch. *J. Phys. Chem. A* **2012**, *116* (14), 3527−3533.

(30) Lumento, F.; Zanirato, V.; Fusi, S.; Busi, E.; Latterini, L.; Elisei, F.; Sinicropi, A.; Andruniów, T.; Ferré, N.; Basosi, R.; et al. Quantum Chemical Modeling and Preparation of a Biomimetic Photochemical Switch. *Angew. Chem., Int. Ed.* **2007**, *46* (3), 414−420.

(31) Sinicropi, A.; Martin, E.; Ryazantsev, M.; Helbing, J.; Briand, J.; Sharma, D.; Léonard, J.; Haacke, S.; Cannizzo, A.; Chergui, M.; et al. An Artificial Molecular Switch That Mimics the Visual Pigment and Completes Its Photocycle in Picoseconds. *Proc. Natl. Acad. Sci. U. S. A.* **2008**, *105* (46), 17642−17647.

(32) Briand, J.; Braem, O.; Rehault, J.; Leonard, J.; Cannizzo, A.; Chergui, M.; Zanirato, V.; Olivucci, M.; Helbing, J.; Haacke, S. Coherent Ultrafast Torsional Motion and Isomerization of a Biomimetic Dipolar Photoswitch. *Phys. Chem. Chem. Phys.* **2010**, *12* (13), 3178−3187.

(33) Léonard, J.; Briand, J.; Fusi, S.; Zanirato, V.; Olivucci, M.; Haacke, S. Isomer-Dependent Vibrational Coherence in Ultrafast Photoisomerization. *New J. Phys.* **2013**, *15*, 105022.

(34) Pagano, K.; Paolino, M.; Fusi, S.; Zanirato, V.; Trapella, C.; Giuliani, G.; Cappelli, A.; Zanzoni, S.; Molinari, H.; Ragona, L.; et al. Bile Acid Binding Protein Functionalization Leads to a Fully Synthetic Rhodopsin Mimic. *J. Phys. Chem. Lett.* **2019**, *10* (9), 2235−2243.

(35) Gueye, M.; Manathunga, M.; Agathangelou, D.; Orozco, Y.; Paolino, M.; Fusi, S.; Haacke, S.; Olivucci, M.; Léonard, J. Engineering the Vibrational Coherence of Vision into a Synthetic Molecular Device. *Nat. Commun.* **2018**, *9* (1), 313.

(36) Gueye, M.; Paolino, M.; Gindensperger, E.; Haacke, S.; Olivucci, M.; Léonard, J. Vibrational Coherence and Quantum Yield of Retinal-Chromophore-Inspired Molecular Switches. *Faraday Discuss.* **2020**, *221*, 299−321.

(37) Schapiro, I.; Gueye, M.; Paolino, M.; Fusi, S.; Marchand, G.; Haacke, S.; Martin, M. E.; Huntress, M.; Vysotskiy, V. P.; Veryazov, V.; et al. Synthesis, Spectroscopy and QM/MM Simulations of a

Biomimetic Ultrafast Light-Driven Molecular Motor. *Photochem. Photobiol. Sci.* **2019**, *18* (9), 2259−2269.

(38) Marchand, G.; Eng, J.; Schapiro, I.; Valentini, A.; Frutos, L. M.; Pieri, E.; Olivucci, M.; Léonard, J.; Gindensperger, E. Directionality of Double-Bond Photoisomerization Dynamics Induced by a Single Stereogenic Center. *J. Phys. Chem. Lett.* **2015**, *6* (1), 599−604.

(39) Paolino, M.; Gueye, M.; Pieri, E.; Manathunga, M.; Fusi, S.; Cappelli, A.; Latterini, L.; Pannacci, D.; Filatov, M.; Léonard, J.; et al. Design, Synthesis, and Dynamics of a Green Fluorescent Protein Fluorophore Mimic with an Ultrafast Switching Function. *J. Am. Chem. Soc.* **2016**, *138* (31), 9807−9825.

(40) Cornell, W. D.; Cieplak, P.; Bayly, C. I.; Gould, I. R.; Merz, K. M.; Ferguson, D. M.; Spellmeyer, D. C.; Fox, T.; Caldwell, J. W.; Kollman, P. A. A Second Generation Force Field for the Simulation of Proteins, Nucleic Acids, and Organic Molecules. *J. Am. Chem. Soc.* **1995**, *117* (19), 5179−5197.

(41) Lipparini, F.; Cappelli, C.; Barone, V. Linear Response Theory and Electronic Transition Energies for a Fully Polarizable QM/ Classical Hamiltonian. *J. Chem. Theory Comput.* **2012**, *8* (11), 4153− 4165.

(42) Cappelli, C. Integrated QM/Polarizable MM/Continuum Approaches to Model Chiroptical Properties of Strongly Interacting Solute-Solvent Systems. *Int. J. Quantum Chem.* **2016**, *116* (21), 1532− 1542.

(43) Giovannini, T.; Egidi, F.; Cappelli, C. Molecular Spectroscopy of Aqueous Solutions: A Theoretical Perspective. *Chem. Soc. Rev.* **2020**, *49* (16), 5664−5677.

(44) Giovannini, T.; Egidi, F.; Cappelli, C. Theory and Algorithms for Chiroptical Properties and Spectroscopies of Aqueous Systems. *Phys. Chem. Chem. Phys.* **2020**, *22* (40), 22864−22879.

(45) Giovannini, T.; Olszòwka, M.; Cappelli, C. Effective Fully Polarizable QM/MM Approach To Model Vibrational Circular Dichroism Spectra of Systems in Aqueous Solution. *J. Chem. Theory Comput.* **2016**, *12* (11), 5483−5492.

(46) Giovannini, T.; Del Frate, G.; Lafiosca, P.; Cappelli, C. Effective Computational Route towards Vibrational Optical Activity Spectra of Chiral Molecules in Aqueous Solution. *Phys. Chem. Chem. Phys.* **2018**, *20* (14), 9181−9197.

(47) Mennucci, B.; Cammi, R.; Tomasi, J. Excited States and Solvatochromic Shifts within a Nonequilibrium Solvation Approach: A New Formulation of the Integral Equation Formalism Method at the Self-Consistent Field, Configuration Interaction, and Multi-configuration Self-Consistent Field Level. *J. Chem. Phys.* **1998**, *109* (7), 2798−2807.